

Modeling phase transformations in Mn-rich disordered rocksalt cathodes with charge-informed machine-learning interatomic potentials

Peichen Zhong,^{1,2,*} Bowen Deng,^{1,2} Shashwat Anand,² Tara Mishra,² and Gerbrand Ceder^{1,2,†}

¹*Department of Materials Science and Engineering,
University of California, Berkeley, California 94720, United States*

²*Materials Sciences Division, Lawrence Berkeley National Laboratory, California 94720, United States*
(Dated: June 26, 2025)

Mn-rich disordered rocksalt (DRX) cathode materials exhibit a phase transformation from a disordered to a partially disordered spinel-like structure (δ -phase) during electrochemical cycling. In this computational study, we used charge-informed molecular dynamics with a fine-tuned CHGNet foundation potential to investigate the phase transformation in $\text{Li}_x\text{Mn}_{0.8}\text{Ti}_{0.1}\text{O}_{1.9}\text{F}_{0.1}$. Our results indicate that transition metal migration occurs and reorders to form the spinel-like ordering in an FCC anion framework. The transformed structure contains a higher concentration of non-transition metal (0-TM) face-sharing channels, which are known to improve Li transport kinetics. Analysis of the Mn valence distribution suggests that the appearance of tetrahedral Mn^{2+} is a consequence of spinel-like ordering, rather than the trigger for cation migration as previously believed. Calculated equilibrium intercalation voltage profiles demonstrate that the δ -phase, unlike the ordered spinel, exhibits solid-solution signatures during the 0-TM to Li_{tet} conversion reaction. A higher Li capacity is obtained than in the DRX phase. This study provides atomic insights into solid-state phase transformation and its relation to experimental electrochemistry, highlighting the potential of charge-informed machine learning interatomic potentials for understanding complex oxide materials.

I. INTRODUCTION

The increasing demand for sustainable energy storage has driven the development of high-energy-density and cost-effective cathode materials for rechargeable Li-ion batteries [1–3]. Disordered rocksalt (DRX) cathodes using manganese (Mn) as the earth-abundant redox-active cation have the potential to scale Li-ion energy storage to several TWh/year [4]. Recent studies demonstrate that initiating a Mn-rich disordered rocksalt structure undergoes an in-situ transformation into a partially disordered spinel-like phase (termed as δ -phase) upon electrochemical cycling, resulting in increased capacity and rate capability for cathode designs [5–9]. This approach mitigates the typical low capacity in other DRX cathodes by promoting a new voltage feature around 4 V and an extended 3 V plateau. Moreover, in contrast to conventional $\text{Li}_x\text{Mn}_2\text{O}_4$ spinel cathodes, which suffer from the two-phase reactions leading to inhomogeneity-induced stresses and mechanical degradation between $0.5 < x < 1$, the δ -phase maintains a single (solid-solution) phase reaction throughout the cycling process. Cai *et al.* [9] demonstrates that such a series of δ -phase material exhibits an impressive capacity of over 280 mAh/g and an energy density exceeding 800 Wh/kg while maintaining minimal voltage decay even after extensive cycling.

The spinel is distinct from the disordered rocksalt based on cation ordering in an FCC anion framework. Figure 1a–1c presents the cation orderings in a conceptualized graph representation as a projection of the 3-dimensional FCC structure shown in Fig. 1c, including

the disordered rocksalt ($\text{Fm}\bar{3}\text{m}$), spinel ($\text{Fd}\bar{3}\text{m}$), and partially disordered spinel (δ -phase) structures. The green and purple spheres represent Li and Mn ions, respectively, occupying the octahedral sites (O_h , denoted as o) of the FCC rocksalt framework. For simplicity, the stoichiometric LiMnO_2 is used for illustration in Fig. 1a–c. The graph edges connect the O_h sites to the interstitial tetrahedral sites (T_d , denoted as t), which are represented by white dashed circles in Fig. 1. In the spinel LiMnO_2 ordering, the octahedral sites are categorized into $16c$ and $16d$ sites as shown in Fig. 1b. All $16c$ sites are occupied by Li, while all $16d$ sites are occupied by Mn. The tetrahedral site neighbored by four $16c$ Li is denoted as an $8a$ site in a spinel. When the spinel is delithiated to $\text{Li}_{0.5}\text{MnO}_2$, the $16c$ sites become vacancies and the $8a$ sites are all occupied by Li. More generally, the tetrahedral site neighbored by four Li is also termed a 0-TM channel. Urban *et al.* [10] demonstrated that long-range connected 0-TM percolating channels are essential for facile Li diffusion in an FCC framework, with the spinel ordering having the highest amount of 0-TM channels in theory. The partially disordered spinel is conceptually illustrated in Fig. 1c as an intermediate state between the spinel and disordered ordering.

The phase transformation from DRX to δ -phase is related to the transition metal (TM) migration of the mobile Mn ion when neighboring cation vacancies are created [11]. The TM can take the pathway connected by the octahedral-tetrahedral-octahedral (o - t - o) sites in an FCC framework. For the migration process, it is typically concluded that Mn migration is strongly coupled with its charge state, Mn^{4+} is generally considered immobile, while Mn^{3+} and Mn^{2+} are considered more mobile according to the nudged-elastic band calculations [12–14]. However, simulating these charge-coupled dynamics has

* zhongpc@berkeley.edu

† gceder@berkeley.edu

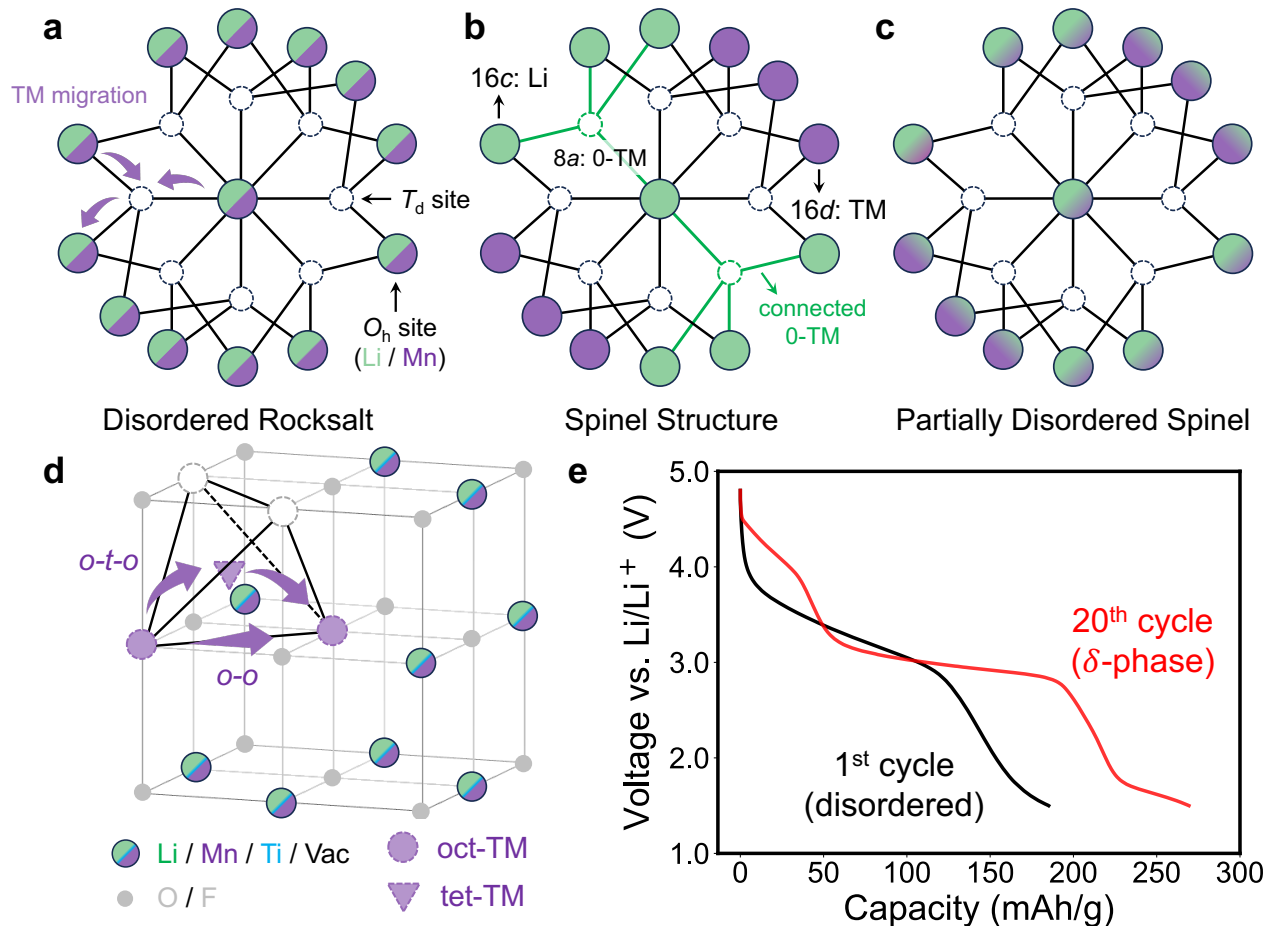


FIG. 1. **Local ordering and electrochemical characteristics in Li-Mn-O-F systems.** (a-c) Schematic representations of local cation ordering in LiMnO_2 : (a) disordered rocksalt, (b) spinel, and (c) partially disordered spinel structures. Green and purple circles represent Li and Mn occupying octahedral (O_h , denoted as o) sites in an FCC rocksalt framework, respectively. Edges connect O_h sites to interstitial tetrahedral sites (T_d , denoted as t). In the spinel structure (b), O_h sites are categorized as $16c$ (Li-occupied) and $16d$ (Mn-occupied). The T_d sites adjacent to $16c$ Li are designated as $8a$ sites in 0-TM channels (without TM neighbors), forming an interconnected percolating network (green lines). The partially disordered spinel structure (c) shows intermediate $16c/16d$ site occupancy between spinel and disordered structures. (d) TM migration pathways in the FCC rocksalt framework: arrows indicate possible migration routes through an intermediate T_d site (o - t - o) or direct connection between O_h sites (o - o). (e) Experimental voltage profiles of $\text{Li}_x\text{Mn}_{0.8}\text{Ti}_{0.1}\text{O}_{1.9}\text{F}_{0.1}$ during cycling between 1.5 and 4.8 V at 20 mA/g, showing the 1st (black line) and 20th (red line) cycles. The 20th cycle reveals a new voltage feature at 4 V and an extended 3 V plateau, indicating δ -phase formation.

long been challenging, as the required time and length scales are inaccessible to conventional *ab initio* methods. Previously, cluster expansion (CE) methods have been shown successfully as a surrogate model of density functional theory (DFT) calculations for modeling the configurational thermodynamics in complex oxides via Monte Carlo (MC) simulation at scale [15–17]. Nonetheless, the limited expressibility and coarse-grained nature of these models render them less adequate for capturing the complex charge-coupled dynamical processes involved in TM migrations [9, 18]. The advent of machine learning interatomic potentials (MLIPs) has opened new avenues for addressing these problems by enabling large-scale and nano-second-long simulations with *ab-initio* quantum ac-

curacy [19–21]. By using magnetic moments as a proxy for atomic charge, Deng *et al.* [21] recently simulated a phase transformation from an orthorhombic to a spinel-like phase in $\text{Li}_{0.5}\text{MnO}_2$ with charge-informed MD. It identified the timescale discrepancies between charge disproportionation and ion hops, suggesting that the emergence of Mn^{2+} is correlated to long-range spinel-like ordering but not solely to the local hopping into the tetrahedral occupancy.

In this study, we extend the computational study of the phase transformation in $\text{Li}_x\text{Mn}_{0.8}\text{Ti}_{0.1}\text{O}_{1.9}\text{F}_{0.1}$ (LMTOF), which is a Mn-rich DRX cathode. We parametrized a CHGNet-MLIP using $r^2\text{SCAN}$ -DFT calculations for various atomic configurations to sample the

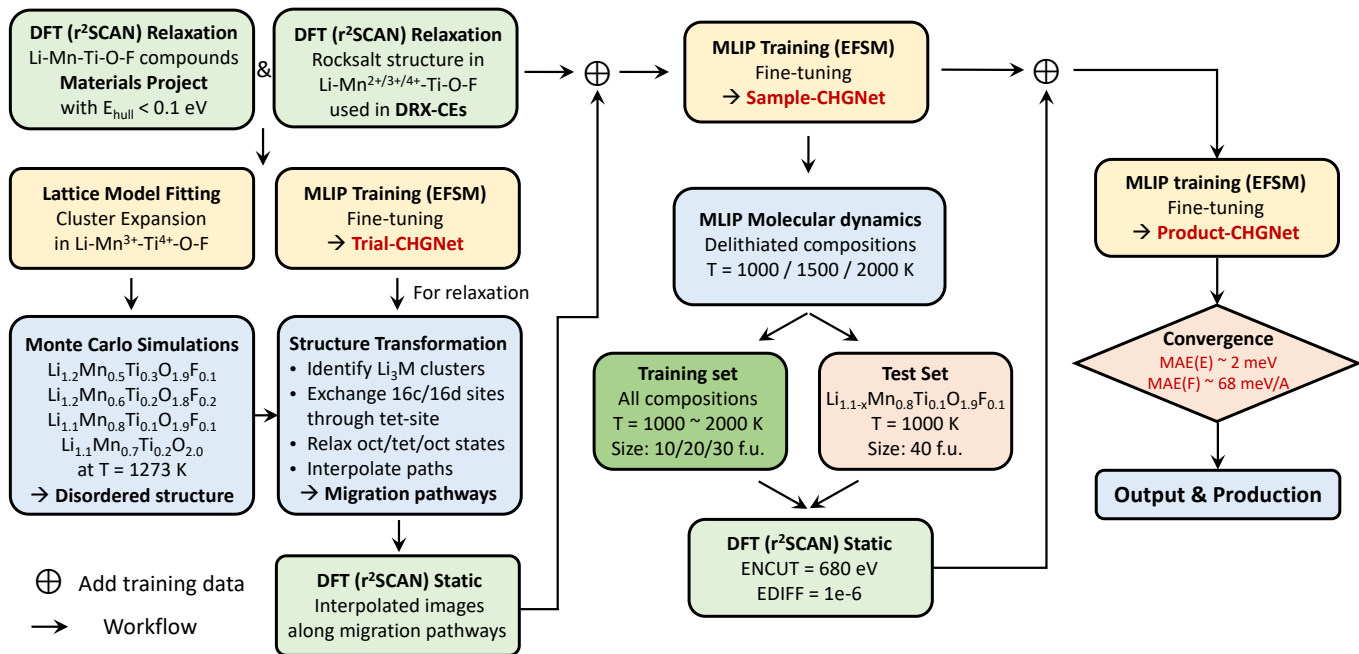


FIG. 2. Flowchart illustrating the development process of fine-tuned CHGNet machine learning interatomic potential (MLIP) and cluster expansion models for the Li-Mn-Ti-O-F system.

potential energy surface in this chemical space. The fine-tuned CHGNet-MLIP was used to implement charge-informed MD simulations starting from a disordered phase in $\text{Li}_{0.6}\text{Mn}_{0.8}\text{Ti}_{0.1}\text{O}_{1.9}\text{F}_{0.1}$. The MD simulations revealed a phase transformation from a disordered rock-salt to a spinel-like (δ) phase. From the magnetic moment predictions, we demonstrate that the Mn migration is mainly contributed by Mn^{3+} at the beginning, while Mn^{2+} collectively emerges as the spinel-like ordering forms. Furthermore, we investigated the impact of this partial disorder on the electrochemical intercalation voltage profiles based on the structures obtained from the MD simulations. Our work provides insights into the application of MLIPs for studying complex energy materials and offers a mechanistic understanding of the partial cation-disorder effect on intercalation electrochemistry at the atomic scale.

II. METHODS

A. Machine learning interatomic potential

To efficiently compute the energy and interatomic forces, we employed the Crystal Hamiltonian Graph Neural Network (CHGNet) as a surrogate model for DFT calculations [21]. CHGNet is a graph-neural-network-based MLIP that utilizes message-passing layers to propagate atomic information via a set of nodes $\{v_i\}$ connected by edges $\{e_{ij}\}$ [22]. After $n - 1$ message-passing layers, the node features $\{v_i^{n-1}\}$ are linearly projected onto magnetic moments by $\phi_m(\cdot)$, and the total energy is calcu-

lated as a sum of non-linear node projections by $\phi_E(\cdot)$ over all atoms $\{v_i^n\}$ with an additional message-passing layer

$$m_i = \phi_m(v_i^{n-1}), \quad E_{\text{tot}} = \sum_i \phi_E(v_i^n). \quad (1)$$

The nodes $\{v_i^{n-1}\}$ are regularized by DFT magnetic moments to carry rich information about both local ionic environments and to serve as a proxy for the atomic charge. The forces and stress are calculated via auto-differentiation of the total energy with respect to the atomic Cartesian coordinates and strain:

$$\vec{f}_i = -\frac{\partial E_{\text{tot}}}{\partial \vec{x}_i}, \quad \boldsymbol{\sigma} = \frac{1}{V} \frac{\partial E_{\text{tot}}}{\partial \boldsymbol{\varepsilon}}. \quad (2)$$

This approach allows CHGNet to capture the complex relationships between charge distributions and energetics with given atomic configurations.

B. Potential energy surface sampling

While CHGNet [21] as a pre-trained foundation potential achieves reasonable performance in predicting materials stability on out-of-distribution datasets [23], recent benchmarks observed a systematic softening of the ML predicted potential energy surface (PES) compared to the DFT ground truth, particularly for atomic configurations from MD simulations with high energy [24, 25]. To improve simulation accuracy, we performed multi-faceted sampling of the PES for the Li-Mn-Ti-O-F chemical space [26], as follows:

Existing dataset – We collected the compounds in the Materials Project database within the Li–Mn–Ti–O–F chemical space that have decomposition energy (energy above the convex hull, E_{hull}) lower than 0.1 eV/atom as a general coverage of such chemical space [27]. Furthermore, we adopted the structures from the training dataset of previously reported cluster expansion (CE) models for DRXs containing Mn²⁺/Mn³⁺ as redox-active species (DRX-CE) [28, 29]. All these structures in the DRX-CE dataset have rocksalt lattices but different cation and anion orderings. These structures were relaxed by DFT calculations. The relaxed structures with rocksalt frameworks were used to fit a cluster expansion Hamiltonian (lattice model fitting, see Appendix B). The relaxation trajectories from structures from the two datasets were used to fine-tune a Trial CHGNet.

Partially disordered structures – Given that existing datasets do not include atomic configurations specifically representing partially disordered structures with spinel-like orderings, we developed a custom sampling procedure to generate these configurations. (1) Monte Carlo (MC) simulations were employed to obtain the disordered rocksalt atomic configurations equilibrate at finite temperatures, which were generated in supercells of the primitive spinel cell (see Appendix B for details).

Given these disordered structures, we compared the occupancy of the spinel supercell and the disordered rocksalt in such a supercell lattice. The octahedral cation sites are categorized into 16c and 16d sites. Under this classification, a random distribution of TM yields the disordered structure, while an increased number of TM occupations on 16d sites indicates more spinel-like ordering.

To generate different degrees of spinel order, we applied site exchanges between the two nearest octahedral sites to transform the disordered structure towards the spinel ordering through either (a) an exchange between a 16c TM and a 16d Li via a Li₃M tetrahedron; or (b) an exchange between a 16d TM and a 16d Li. The (a) step is to create more spinel-like ordering and the (b) step is to exchange the cation ordering within the 16d sites to potentially create more available Li₃M tetrahedron. We assume that TM migration occurs through the *o-t-o* path with no other TM neighbors in the delithiated states (i.e., through the Li₃M tetrahedron, Fig. 3). By iteratively applying site exchanges within different Li₃M tetrahedra, one can obtain a collection of structures ranging from 0% (disordered) to nearly 100% spinel ordering.

TM migration pathways – Since TM migration is a rare, high-energy-barrier event [9], especially for unfavorable valence states like Mn⁴⁺, we implemented a passive sampling approach to effectively model the diffusion kinetics with the following steps:

For each site exchange step via the Li₃M tetrahedron, three different states are generated as A (initial state, TM occupied on O_h site), B (intermediate state, TM occupied on T_h site), and C (final state, TM occupied on O_h site), which are shown in Fig. 3. The other neighboring Li atoms are removed to create vacancies, for which we as-

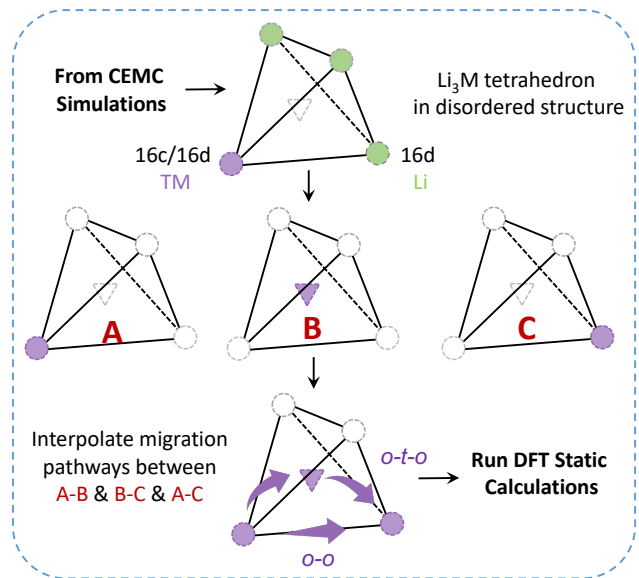


FIG. 3. **Schematic representation of TM migration pathway sampling process.** The procedure consists of three steps: (1) Identification of a Li₃M tetrahedron containing one 16c or 16d TM and one 16d Li; (2) Creation of vacancies by removing Li ions from O_h sites, followed by TM placement at three positions representing the initial (A), intermediate (B), and final (C) states of *o-t-o* migration; (3) Generation of atomic configurations along A-B, B-C, and A-C paths through interpolation, with subsequent evaluation using static DFT calculations.

sume no face-sharing between the migrating TM and O_h cations. The structures in the A/B/C states were relaxed using the Trial-CHGNet fitted with structures from the existing datasets. After structure relaxation, five images interpolated along A-B (*o-t* path) and B-C (*t-o* path) are evaluated with static DFT calculations, analogous to the intermediate states for nudged elastic band (NEB) calculations. Furthermore, we follow the same approach to generate the direct migration from the *o-o* path (A-C) for labeling high-energy and unfavorable states.

In addition, we considered two different delithiation levels for sampling TM migration pathways: (a) A dilute level, where only three Li ions are removed to create a diffusion channel for TM migration (e.g., a pristine supercell structure with Li₄₄Mn₃₂Ti₄O₇₆F₄ yields a delithiated structure with Li₄₁Mn₃₂Ti₄O₇₆F₄). This level allows for the investigation of local TM hopping energetics. (b) A medium delithiation level, where 0.5 Li per formula unit (f.u.) is removed from the structure to create delithiated states (e.g., Li ions are randomly removed to create a structure with Li₂₄Mn₃₂Ti₄O₇₆F₄). This level allows the sampling of delithiated states, representing the charging process in a battery. By sampling partially disordered structures at these two delithiation levels, we include a more comprehensive description of the cation ordering energetics, TM hop, and relevant local environments in which TM hopping occurs at the composition that is en-

ergetically favorable for spinel formation (i.e., the composition close to $\text{Li}_{0.5}\text{TMO}_2$).

By adding the static DFT calculations of these sampled atomic configurations to the relaxation trajectories, another MLIP was parameterized (denoted as Sample-CHGNet) to perform MD simulations for enhanced sampling.

MD trajectories – To further sample the thermally excited atomic configurations at finite temperatures, we employed Sample-CHGNet to perform molecular dynamics (MD) simulations with disordered structures across various compositions. These structures were first generated in the pristine (lithiated) state from the CE-MC simulations at $T = 1273$ K using supercells of $10\times$ and $20\times$ formula units (f.u.), including $\text{Li}_{1.2}\text{Mn}_{0.5}\text{Ti}_{0.3}\text{O}_{1.9}\text{F}_{0.1}$, $\text{Li}_{1.2}\text{Mn}_{0.6}\text{Ti}_{0.2}\text{O}_{1.8}\text{F}_{0.2}$, $\text{Li}_{1.1}\text{Mn}_{0.8}\text{Ti}_{0.1}\text{O}_{1.9}\text{F}_{0.1}$, and $\text{Li}_{1.1}\text{Mn}_{0.7}\text{Ti}_{0.2}\text{O}_{2.0}$. For each disordered structure, three different delithiated levels (removing 0.2/0.4/0.6 Li per f.u. from the pristine structure) were generated to initiate the MD simulations using the Sample-CHGNet. The MD simulations were run at $T = 1000/1500/2000$ K for $t = 1$ ns with a time step of $\Delta t = 2$ fs under NVT ensembles. From each MD trajectory, 200 structures were randomly sampled, and their energies were calculated using static DFT and added to the training set. In addition to the training set, we further ran CHGNet-MD simulations in NVT ensembles at $T = 1000$ K using Sample-CHGNet with a supercell of $\text{Li}_{44-x}\text{Mn}_{32}\text{Ti}_4\text{O}_{76}\text{F}_4$ ($40\times$ f.u.). These trajectories were further evaluated by $r^2\text{SCAN-DFT}$ static calculations and were set as the test set.

The final CHGNet for production (denoted as Product-CHGNet) was fine-tuned using all structures in the training set (including 88,852 structures) starting from the pretrained model. It achieved a convergence of 2 meV/atom in energy, 68 meV/Å in force, 0.086 GPa in stress, and 0.019 μ_B in magnetic moment for the test error. A summary flowchart is illustrated in Fig. 2 to describe the whole procedure.

III. RESULTS

To investigate the structural evolution, we performed charge-informed molecular dynamics from the disordered structure to monitor the phase change to the δ -phase. The initial (disordered) structure was generated by sampling from the equilibrium ensemble of CE-MC simulations at $T = 1273$ K. The MC structure represents the pristine (lithiated) composition ($\text{Li}_{1.1}\text{Mn}_{0.6}\text{Ti}_{0.1}\text{O}_{1.9}\text{F}_{0.1}$) with a supercell containing 320 atoms. Based on the pristine structure, a delithiated structure ($\text{Li}_{0.5}\square_{0.6}\text{Mn}_{0.6}\text{Ti}_{0.1}\text{O}_{1.9}\text{F}_{0.1}$, where \square represents cation vacancy) was then obtained by randomly removing Li ions and relaxing the delithiated configuration using the Product-CHGNet with a force convergence criterion of < 0.1 eV/Å. After relaxation, MD simulations were subsequently performed for $t = 2$ ns with a time

step of $\Delta t = 2$ fs under the NVT ensemble at $T = 1273$ K. The MD trajectories were collected for subsequent structural analysis.

A. Structure ordering analysis

Figure 4a presents the simulated X-ray diffraction (XRD) patterns derived from the structures within the time interval of $t = 0$ to $t = 2$ ns. To analyze the evolution of cation ordering on the FCC lattice, the atomic positions from the MD snapshots were refined to their nearest ideal Wyckoff sites. The gray dashed lines in Fig. 4a denote the characteristic peaks of spinel ordering (18° , 35° , etc.). At the onset of the MD simulation ($t = 0$ ns), there are no obvious peaks indicating spinel ordering. After approximately $t = 0.6$ ns, the intensity of the spinel peaks increases and becomes more significant in subsequent time scales as the MD simulation proceeds, suggesting the formation of the spinel-like δ -phase.

Figure 4b illustrates the energy landscape across the simulated MD trajectories. The black points denote the potential energies, while the colored points represent the total energies. The energies are depicted relative to their values at the initial state. A notable decrease in energy (approximately 60 meV/anion) is observed for the δ -phase following a $t = 2$ ns MD simulation. This energy reduction indicates that spinel-like cation ordering is thermodynamically favored at the composition $\text{Li}_{0.6}\text{Mn}_{0.8}\text{Ti}_{0.1}\text{O}_{1.9}\text{F}_{0.1}$ when sufficient cation vacancies are present. This thermodynamic preference for spinel-like ordering aligns with previous computational studies that demonstrated the stability of spinel structures in Li-Mn-O systems, such as $\text{Li}_{0.5}\text{MnO}_2$ [30].

To study the change in local cation ordering, we analyzed the short-range order (SRO) indicated by the tetrahedron occupancy as a function of MD simulation time. Figure 4c presents the occurrence of 0-TM (solid green line) and 1-TM tetrahedral (solid purple line) channels in the MD structure, as a ratio to all interstitial tetrahedral sites. The 0-TM channel has a low migration barrier that kinetically favors fast Li-ion transport [31]. To compare with disordered phases, the dashed green lines in Fig. 4c indicate the random limit of the 0-TM channel for two Li contents (~ 0.06 for $\text{Li}_{1.0}$ and ~ 0.09 for $\text{Li}_{1.1}$ at the fully lithiated level) for reference. At the beginning of the MD simulation ($t = 0$ ns), the occurrence of 0-TM channels is approximately 0.03. This value is significantly lower than that of the random limit of $\text{Li}_{1.1}\text{TMO}_2$ (0.09), where the value is estimated based on a rocksalt structure with 0.1 excess Li and fully random cation ordering. The low value of 0-TM content in the initial structure indicates reduced percolating Li content and suggests that SRO is unfavorable for long-range Li percolation, which is consistent with previous predictions in Mn-Ti-based DRXs [28, 29]. As the phase transformation progresses, the occurrence of 0-TM channels increases, reaching approximately 0.06 after $t = 2$ ns of MD simulation. This rise in

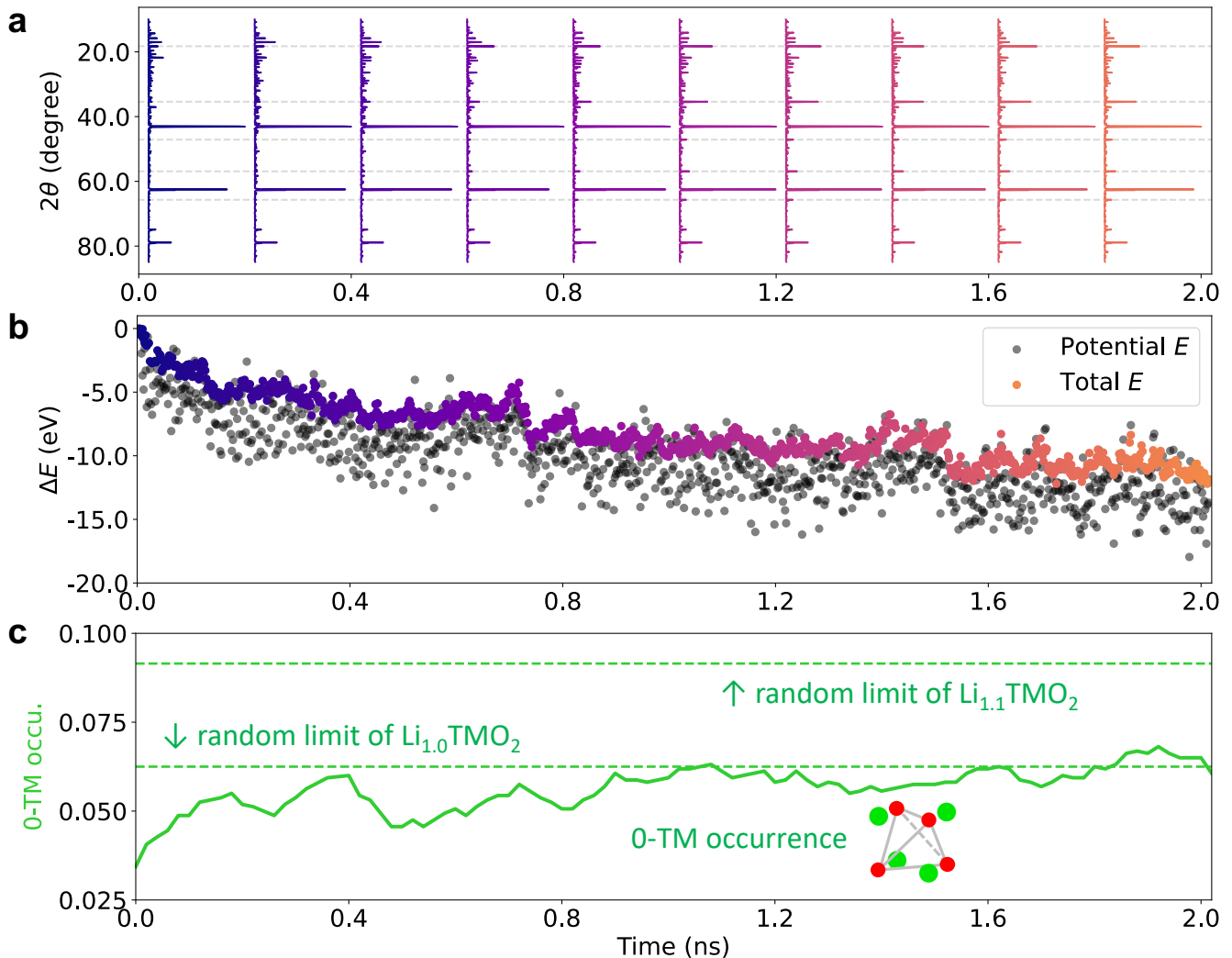


FIG. 4. **Structural and energetic analysis from the MD simulation.** (a) Simulated X-ray diffraction (XRD) patterns of the refined structures, with gray dashed lines indicating characteristic spinel ordering peaks (18° , 35° , etc.). (b) Energy evolution showing potential energy (black dots) and total energy (colored dots) relative to the initial structure, normalized per anion. (c) Evolution of tetrahedral channel types (0-TM, green; 1-TM, purple) per formula unit, with green dashed lines indicating reference 0-TM channel occurrence in random $\text{Li}_{1.0}\text{TMO}_2$ and $\text{Li}_{1.1}\text{TMO}_2$ structures.

the number of 0-TM channels agrees with the high 0-TM content in the spinel structure, indicating the emergence of spinel-like ordering.

B. Charge distribution with ion rearrangement

To understand the correlation between Mn migration and its heterovalent state [9, 32], we inferred atomic charge states from the magnetic moments predicted by CHGNet. Figure 5a presents the site-wise distribution of magnetic moments for Mn ions. The heterovalent states of Mn are categorized as follows: $\text{Mn}^{2+} \in [4.1\mu_B, 5.0\mu_B]$, $\text{Mn}^{3+} \in [3.25\mu_B, 4.1\mu_B]$, and $\text{Mn}^{4+} \in [2.5\mu_B, 3.25\mu_B]$. At the beginning of the MD simulation, Mn predomi-

nantly exists in valence states of +3 and +4. As the phase transformation progresses, the concentration of Mn^{2+} gradually increases, as shown by the increased frequency of the highlighted circles in Fig. 5a, particularly after the emergence of spinel-like ordering from 0.6 to 2.0 ns.

For a detailed description of Mn migration conditioned on its valence state, the occupancy of $\text{Mn}_{\text{tet}}^{3+}$ and $\text{Mn}_{\text{tet}}^{2+}$ per f.u. is plotted in Fig. 5b as an indication of hopping events to tetrahedral sites. Although previous nudged elastic band calculations reveal that Mn^{2+} has a lower migration barrier [9, 11], the atomic charges predicted by CHGNet show that most of the tetrahedral Mn are $\text{Mn}_{\text{tet}}^{3+}$ from $t = 0$ to 0.6 ns during the MD simulation. This suggests that Mn^{3+} may migrate without the need for charge disproportionation ($2\text{Mn}^{3+} \rightarrow \text{Mn}^{2+} + \text{Mn}^{4+}$) as proposed by Reed *et al.* [11]. The rise in $\text{Mn}_{\text{tet}}^{2+}$ ap-

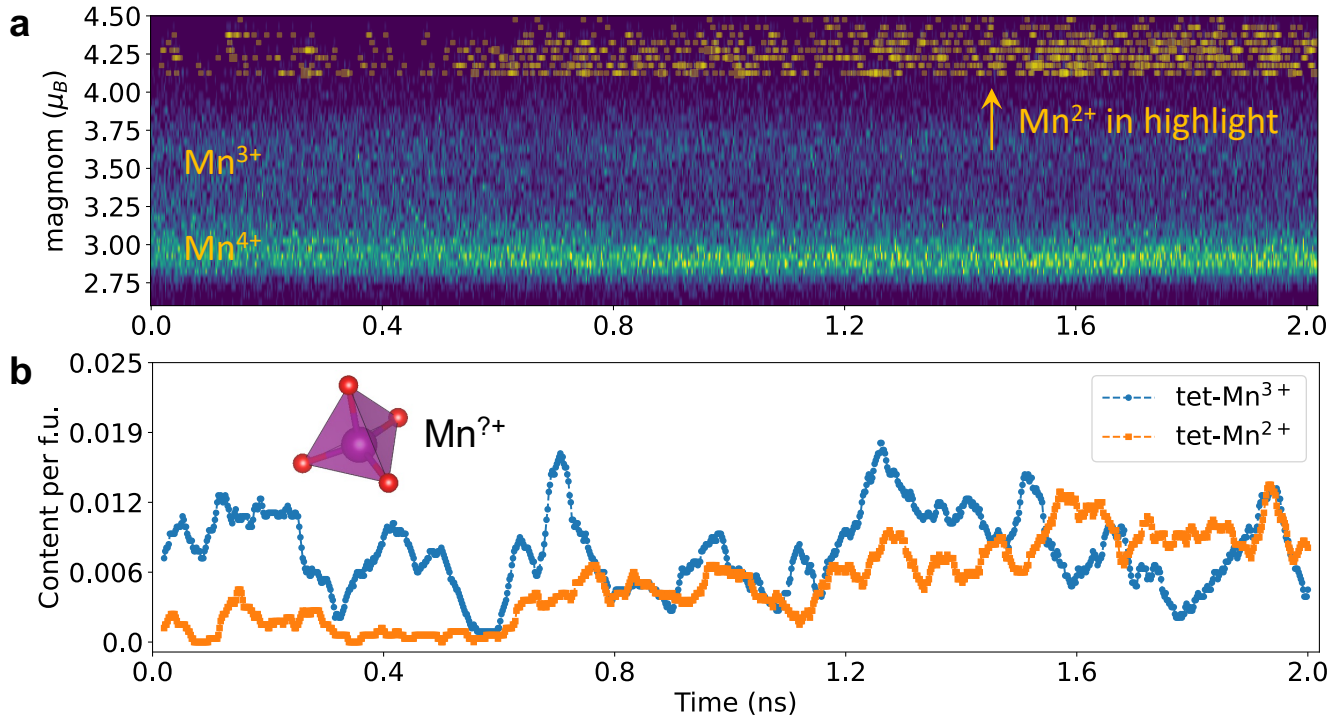


FIG. 5. **Atomic charge analysis of Mn from the MD simulation and magnetic moment prediction.** (a) Time-resolved histogram of magnetic moments for all Mn ions, with brighter colors indicating higher Mn ion populations at given magnetic moment values. Yellow circles highlight the Mn^{2+} distribution. Heterovalent states are categorized as $Mn^{2+} \in [4.1\mu_B, 5.0\mu_B]$, $Mn^{3+} \in [3.25\mu_B, 4.1\mu_B]$, and $Mn^{4+} \in [2.5\mu_B, 3.25\mu_B]$. (b) Temporal evolution of charge-decorated Mn occupancy on tetrahedral sites, showing Mn^{3+} (blue line) and Mn^{2+} (orange line) content per formula unit. The increase in tetrahedral Mn^{2+} after ~ 0.6 ns coincides with spinel-like ordering formation.

pears after around $t = 0.6$ ns, which corresponds to the formation of spinel characteristic peaks (18° , 35°) in Fig. 4a. This evidence suggests that Mn^{3+} migration initiates the transformation before long-range spinel-like order is established. The subsequent emergence of tetrahedral Mn^{2+} appears to be a consequence of this long-range ordering (ns-scale) rather than a prerequisite for local cation hops (ps-scale). The simulation results are consistent with previous MD simulations of the Li_xMnO_2 phase transformation revealed by Deng *et al.* [21] using the GGA+ U -based MLIP.

C. Intercalation voltage profile of δ -phase

To evaluate the effect of partial disorder on the electrochemical performance of the transformed structure from MD, we computed the intercalation voltage profiles using Product-CHGNet. We focused on two characteristic reactions in an ordered spinel Li_xMnO_2 : (1) a 0-TM conversion reaction at a lower voltage, where the occupancies of Li ions are transformed from the 16c octahedral sites to the 8a tetrahedral sites collectively:



and (2) a $Li_{\text{tet}} \rightarrow \Box_{\text{tet}}$ conversion at a higher voltage, where Li is intercalated on the 8a site. It is important to note that Eq. (3) is defined for an independent 0-TM channel (i.e., one that does not share Li with another tetrahedral channel). In an ordered $LiMnO_2$ spinel, each Li_{oct} is face-sharing with two 0-TM channels, where removing one Li from such a 0-TM channel results in a high defect energy [18]. The delithiation is, therefore, a collective conversion that exhibits a two-phase reaction between $Li_{0.5}MnO_2$ and $LiMnO_2$ with a characteristic 3 V voltage plateau [33].

Using Eq. (3), we enumerated different Li-vacancy configurations with fixed TMs and an anion framework (topotactically) at each (de)lithiation level based on the MD structure. The Product-CHGNet was used to perform structure relaxation for both lithiation and delithiation paths (see Appendix C for details). The energies of these (de)lithiated structures were used to construct the convex hull and the corresponding voltage profile as shown in Fig. 6a and Fig. 6b (see Methods).

For the region with high Li concentration ($0.5 \leq x \leq 1.1$), the 0-TM to Li_{tet} conversion exhibits nearly solid-solution behavior, as evidenced by the convex hull being connected by several ground states in Fig. 6a. Particularly, for the early stage of delithiation ($0.7 < x < 1.1$),

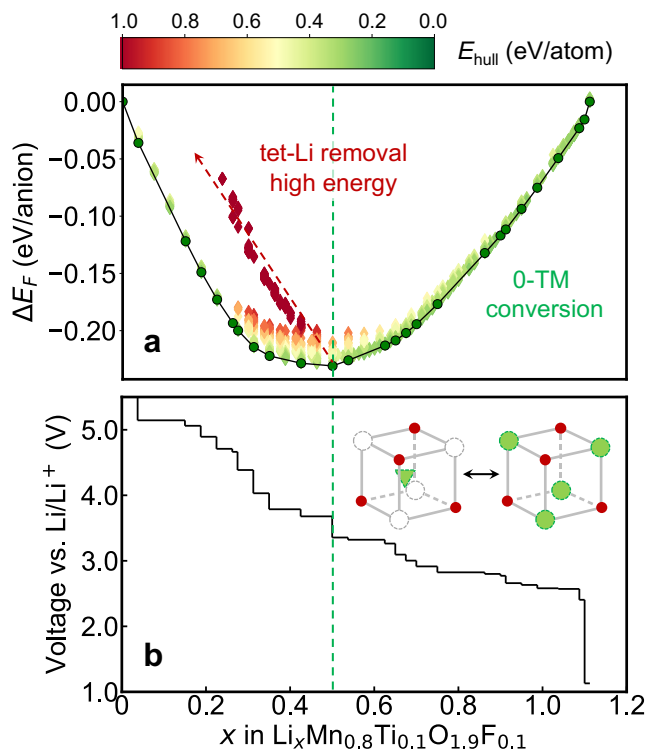


FIG. 6. **Phase diagram and intercalation voltage profiles of LMTOF in the δ -phase.** (a) Phase diagram where each point represents a Li-vacancy configuration, with color indicating energy above the convex hull in the black line. The color bar indicates the energy above the convex hull. Ground states on the convex hull are marked with green circles. The dark red arrow indicates high formation energy (ΔE_F) for direct removal of Li_{tet} when $x \leq 0.5$. (b) Voltage profiles derived from the convex hull, showing nearly solid-solution behavior for $0.5 \leq x \leq 1.1$ during 0-TM to Li_{tet} conversion. The inset shows the 4Li_{oct} (0-TM) $\rightarrow \text{Li}_{\text{tet}}$ conversion reaction scheme used to evaluate high Li content intercalation (green spheres = Li cations, red spheres = O/F anions).

the voltage exhibits a flat plateau with a minor slope, indicating that the delithiation through Eq. (3) occurs in similar local chemical environments and exhibits similar chemical potentials (voltages). We found that the voltage at $x = 1.1$ is around 2.40 V, which is slightly lower than the experimental value. This discrepancy is likely attributable to the residual self-interaction error common in DFT functionals, even for $r^2\text{SCAN}$, when a Hubbard U correction is not applied [34, 35]. Although the SCAN-based functional removes more self-interaction than previous LDA and GGA functionals [36], it does not fully remove it and underestimates the intercalation voltage, which is consistent with previous reports [17, 18].

Upon reaching $x = 0.5$, lithium occupies all tetrahedral 0-TM channels (Li_{tet}) in addition to the octahedral Li_{oct} not in the 0-TM channels. Two competing delithiation processes are available, involving either the removal of Li_{tet} or Li_{oct} . We computed both pathways and found

that the low-energy configurations near the convex hull within the range $0.25 \leq x \leq 0.5$ correspond to the removal of Li_{oct} , while the high-energy configurations (represented by dark red markers in Fig. 6a) correspond to the removal of Li_{tet} . These results indicate that even in a structure with partial spinel ordering, Li_{oct} has a preference for delithiation before Li_{tet} . In contrast, the delithiation in spinel Li_xMnO_2 for $0 \leq x \leq 0.5$ entirely corresponds to the removal/insertion of Li_{tet} with a ~ 4 V plateau. We also observe a voltage increase of ~ 0.32 V around $x = 0.5$ (the end of 0-TM to Li_{tet} conversion). The magnitude is not as large as that in spinel LiMnO_2 (> 1.0 V) or in the spinel-ordered $\text{Li}_x\text{Mn}_{0.8}\text{Ti}_{0.1}\text{O}_{1.9}\text{F}_{0.1}$ (see Fig. 7c), suggesting the absence of two-phase reactions in the δ -phase and less inhomogeneity that could lead to battery performance degradation.

To further demonstrate the effect of partial disorder, we evaluated the intercalation voltage profiles of $\text{Li}_{1.1}\text{Mn}_{0.8}\text{Ti}_{0.1}\text{O}_{1.9}\text{F}_{0.1}$ in both the DRX and spinel phases for comparison. The DRX structure was selected from the structure derived from the CE-MC simulations (i.e., the configuration at $t = 0$ s in the MD simulation). The spinel $\text{Li}_{1.1}\text{Mn}_{0.8}\text{Ti}_{0.1}\text{O}_{1.9}\text{F}_{0.1}$ was generated through another CE-MC simulation without exchanges between the $16c$ and $16d$ sites, where all $16c$ sites are occupied by $\text{Li}_{1.0}$ and $16d$ sites are occupied by $\text{Mn}_{0.8}$, $\text{Ti}_{0.1}$, and $\text{Li}_{0.1}$. The MC simulation allows site exchange within $16d$ sites and anion sites, which is designed to capture the underlying SRO of anions and cations in DRXs (e.g., Li-F SRO) [37]. The intercalation at high Li content in both DRX and spinel phases only included the 0-TM conversion reaction as described in Eq. (3).

Figure 7a and 7b illustrate the formation energy convex hull and the voltage profile of the DRX phase, with the δ -phase plotted as a red line for comparison. Due to the insufficient number of 0-TM channels in the DRX structure, a relatively limited Li capacity from the 0-TM conversion is achieved (approximately 0.3 per f.u., as denoted by the green dashed line in Fig. 7a and 7b). The absence of spinel-like ordering results in a profile marked by a mildly steep increase as delithiation progresses. Notably, the overall voltage profile between $0.3 < x < 1.1$ of the DRX phase is higher than that of the δ -phase, suggesting a restricted amount of accessible capacity within an operational voltage window, particularly the capacity around ~ 3 V [8, 9]. In contrast, Figure 7b depicts the calculated results for spinel $\text{Li}_x\text{Mn}_{0.8}\text{Ti}_{0.1}\text{O}_{1.9}\text{F}_{0.1}$. The voltage profile clearly displays a two-phase reaction between $\text{Li}_{1.1}$ and $\text{Li}_{0.6}$ with a linear convex hull in Fig. 7c. Due to the absence of disorder, the spinel phase exhibits a lower average voltage with a two-phase reaction between $0.6 < x < 1.1$, with a voltage step more than 1 V presented at the end of 0-TM conversion. For $x < 0.4$, the intercalation corresponds to $\text{Li}_{\text{tet}} \rightarrow \square_{\text{tet}}$, which shows a similar high-voltage feature as the δ -phase. The effect of cation disorder on the spinel structure demonstrated in our simulations is in full agreement with the previous findings on the cation disorder effects in LiMnO_2 spinel

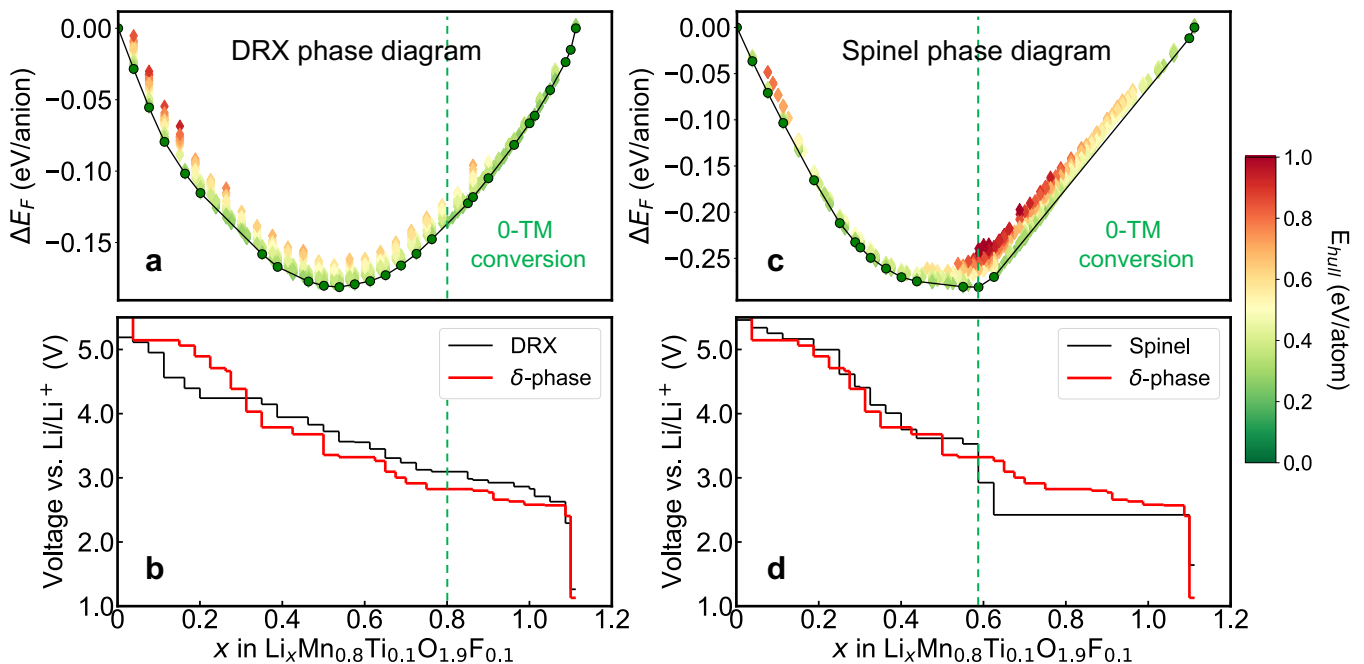


FIG. 7. **Phase diagram and intercalation voltage profiles of LMTOF in DRX and spinel structures.** (a) Formation energy convex hull of the DRX structure, with points representing Li-vacancy configurations colored by energy above the convex hull. (b) DRX LMTOF voltage profile constructed from convex hull ground states, compared with δ -phase profile (red line). Green dashed line indicates Li capacity from 4Li_{oct} (0-TM) \rightarrow Li_{tet} conversion reaction. (c) Formation energy convex hull of the spinel structure using the identical color scheme as (a). (d) Spinel voltage profile showing two-phase reaction between $\text{Li}_{1.1}$ and $\text{Li}_{0.6}$ compositions, evidenced by the linear convex hull in (c) and flat voltage plateau in (d). The spinel LMTOF exhibits a > 1 V voltage step near $\text{Li}_{0.6}$, while the δ -phase (red line) shows solid-solution behavior.

by Chen *et al.* [18].

IV. DISCUSSION

In the evolving landscape of modern battery materials, the complexity of components and configurations exemplified by DRX cathode materials necessitates advanced computational models. Particularly, Mn-rich DRXs exhibit a phase transformation to a partially disordered spinel phase (δ -phase) via in situ electrochemical cycling [8, 9, 38] or chemical delithiation [39]. This transformation is challenging for conventional modeling approaches to capture, particularly the kinetic pathways of TM migration in such a complex oxide. While *ab initio* molecular dynamics could theoretically address this issue, its $\mathcal{O}(N^3)$ computational cost renders it impractical for probing large systems or long timescales. Alternatively, kinetic Monte Carlo (kMC) methods with CE models have been proposed to model cation ordering changes in both cathodes and solid electrolytes [40, 41]. However, parameterizing CEs for disordered oxides/oxyfluorides and accurately calculating migration barriers in diverse local environments remains a non-trivial endeavor [42].

To address these challenges, we fine-tuned a charge-informed foundation MLIP with sampled $r^2\text{SCAN-DFT}$ calculated energies, forces, stresses, and magnetic mo-

ments. The multi-step PES sampling captures the complex interactions from diverse chemical environments and heterovalent states of TMs. Our MD simulations using the fine-tuned CHGNet successfully captured the phase transition from a disordered to a spinel-like configuration in $\text{Li}_{0.6}\text{Mn}_{0.8}\text{Ti}_{0.1}\text{O}_{1.9}\text{F}_{0.1}$.

The simulations reveal that the formation of the δ -phase promotes the occurrence of 0-TM channels, which play a crucial role in facilitating long-range Li-ion transport, whereas the DRX phase exhibits limited availability of these channels. This result agrees with the improved high-rate performance observed in experiments [8, 9, 39]. By analyzing the electrochemical intercalation voltage profiles of the δ -phase and comparing them to those of the DRX and spinel phases, two conclusions can be drawn from the simulation results: (1) The presence of partial cation disorder in the δ -phase effectively eliminates the two-phase reaction, as evidenced by the absence of a sharp voltage increase after $\sim \text{Li}_{0.5}$ removal (see Fig. 7c). (2) The introduction of spinel-like ordering increases the 0-TM occurrence (as indicated by the increased number of 0-TM channels in Fig. 4c) and thus expands the available Li capacity from the 0-TM to Li_{tet} conversion reaction around 3 V (denoted by the green dashed line in Fig. 6b). The Li capacity from 0-TM to Li_{tet} conversion is even higher than that of the spinel in Fig. 5c since the 0-TM channels in partially disordered

phases are less correlated with each other compared to the spinel, where each Li_{oct} is shared by two 0-TM channels.

Although this study represents an integrated investigation of phase transformation in complex oxides combining MC simulations for configurational thermodynamics and MLIP-MD simulations for kinetic modeling, several limitations were identified that could be further addressed in future studies. For example, while our MLIP enables nanosecond-scale or million-atoms simulations with *ab initio* accuracy [43], many important physical processes—such as the formation of anti-phase boundaries in the δ -phase [39] or phase segregation in Li_xFePO_4 cathodes [44]—occur on timescales still beyond this reach. Achieving *ab initio* accuracy while enabling simulations beyond typical MD timescales (such as using generative models for dynamic trajectories) holds promise for investigating these processes [45–47]. Regarding model fine-tuning, recent advances such as active learning with Bayesian force fields [48], stratified sampling from MLIP-driven MD [49], and diffusion-based generative models for mapping reaction pathways [50] provide more efficient sampling techniques beyond the passive sampling implemented in this work, which could enhance MLIP training accuracy by exploring the PES more effectively.

In summary, we demonstrated the application of charge-informed MLIP to model the complex phase transformation from DRX to spinel-like δ -phase in Li-Mn-Ti-O-F systems. The MLIP-MD simulations revealed the mechanism of spinel-like ordering formation and its effect on electrochemical properties. As computational capabilities and new methodologies emerge—particularly in accelerating MLIP simulations and in generative modeling—these advances will pave the way for more accurate and efficient modeling of phase transformations in next-generation energy storage materials.

V. ACKNOWLEDGMENTS

This work was primarily supported by the U.S. Department of Energy, Office of Science, Office of Basic Energy Sciences, Materials Sciences and Engineering Division under Contract No. DE-AC0205CH11231 (Materials Project program KC23MP), and the Assistant Secretary for Energy Efficiency and Renewable Energy, Vehicle Technologies Office, under the Advanced Battery Materials Research (BMR) Program of the US Department of Energy (DOE) under contract No. DE-AC0205CH11231. The computational modeling in this work was supported by the computational resources provided by the Extreme Science and Engineering Discovery Environment (XSEDE), supported by National Science Foundation grant number ACI1053575; the National Energy Research Scientific Computing Center (NERSC); and the Lawrence computational cluster resource provided by the IT Division at the Lawrence Berkeley National Laboratory. The authors thank Zijian Cai for the

valuable discussions.

Appendix A: DFT Calculations

All DFT calculations were performed with the VASP package using the projector-augmented wave method [51, 52], a plane-wave basis set with an energy cutoff of 680 eV, and a reciprocal space discretization of 25 k -points per \AA^{-3} . The calculations were converged to 10^{-6} eV in total energy for electronic loops and 0.02 eV/ \AA in interatomic forces for ionic loops. The regularized strongly constrained and appropriately normed meta-GGA exchange-correlation functional (r²SCAN) [36, 53] was used with consistent computational settings as MPScanRelaxSet [54].

Appendix B: Cluster Expansion & Monte Carlo

The cluster expansion (CE) method [55] is used to study the configurational thermodynamics of materials in which sites can be occupied by multiple cations, and has been applied to study the Li-vacancy intercalation chemistry in layered and disordered materials [17, 56]. The CE expands the energy as a sum of many-body configurational interactions:

$$E(\boldsymbol{\sigma}) = \sum_{\beta} m_{\beta} J_{\beta} \langle \Phi_{\alpha \in \beta} \rangle_{\beta} + \frac{E_0}{\epsilon_r}, \quad \Phi_{\alpha} = \prod_{i=1}^N \phi_{\alpha_i}(\sigma_i) \quad (\text{B.1})$$

A configuration $\boldsymbol{\sigma}$ represents a specific occupancy state of species its allowed sites, and σ_i describes which species sit on the i -th site of the lattice. The cluster basis function $\Phi_{\alpha} = \prod_{i=1}^N \phi_{\alpha_i}(\sigma_i)$ is the product of site basis functions $\phi_{\alpha_i}(\sigma_i)$ across a collection α of multiple sites [57]. The average is taken over the crystal symmetry orbits β , forming a complete basis to expand the energy function in the configuration space. The expansion coefficients J_{β} are called effective cluster interactions (ECIs). The electrostatic energy (Ewald energy E_0/ϵ_r) is included to capture long-range electrostatic interactions (E_0 is the unscreened electrostatic energy, and $1/\epsilon_r$ is fitted as one of the ECIs).

For the simulation of atomic orderings, a cluster-expansion Hamiltonian was generated in the chemical space of $\text{Li}^{+}\text{-Mn}^{3+}\text{-Ti}^{4+}\text{-O}^{2-}\text{-F}^{-}$, with pair interactions up to 7.1 \AA , triplet interactions up to 4.0 \AA , and quadruplet interactions up to 4.0 \AA based on a primitive cell of the rocksalt structure with lattice parameter $a = 3 \text{\AA}$. In total, 83 ECIs (including the constant term J_0) were defined, and the CE Hamiltonian was fitted with 322 unique structures. The ECIs were determined with the optimal sparseness and prediction error (with 69 non-zero elements and < 8 meV/atom) with an $\ell_0\ell_2$ -norm regularized regression [58]. We refer readers to Ref. [59] for details of CE in ionic systems. The CE constructions

were performed using `smol` [60] and `pymatgen` for structure processing [61]. Metropolis–Hastings algorithm was used to sample the atomic configurations from the equilibrium canonical ensemble in CE-MC simulations.

Appendix C: Li-vacancy phase diagram

To construct the simplified intercalation voltage profile calculations, we used an enumeration method for the generation of the delithiated structure and the construction of Li-vacancy phase diagrams. For each delithiation step as an example, it follows:

(1) Select an initial structure with composition $\text{Li}_{x_1}\text{TMO}_2$, relax the structure using the product-CHGNet, and obtain the internal energy $E_{\text{Li}_{x_1}\text{TMO}_2}$.

(2) Generate 20 different delithiated structures, each with a different vacancy occupancy and composition $\text{Li}_{x_2^i}\text{TMO}_2$ (x_2^i may not be equal for all $\{i\}$ structures for the 0-TM to Li_{tet} conversion). This generation process is referred to as an *intercalation step*.

(3) Relax these 20 structures using Product-CHGNet and obtain their internal energies $E_{\text{Li}_{x_2^i}\text{TMO}_2}$ (i denotes

the index of each structure).

(4) The proposed next delithiated structure is chosen based on the minimum voltage with respect to the initial structure $\text{Li}_{x_1}\text{TMO}_2$ using the following equation:

$$\bar{V}(x_1, x_2) \approx -\frac{E_{\text{Li}_{x_1}\text{TMO}_2} - E_{\text{Li}_{x_2}\text{TMO}_2} - (x_1 - x_2)E_{\text{Li}}}{F(x_1 - x_2)}, \quad (\text{C.1})$$

where E_{Li} is the internal energy of the bcc Li metal, and $E_{\text{Li}_x\text{TMO}_2}$ represents the internal energy of the (de)lithiated structures.

(5) Use the i -th structure with the lowest voltage as a start and repeat Step 1 until all possible intercalation steps are consumed.

For the lithiation process, the selection criterion is changed to find the lithiated structure with the maximum voltage. It is important to note that different 0-TM channels may share the same Li atoms in an FCC framework and therefore the conversion of different 0-TM to Li_{tet} thus may result in delithiated structures with varying Li concentrations in Step (2). It is more appropriate to use the minimum/maximum voltage as a selection criterion rather than the energy itself for suggesting the next step in the enumeration method.

-
- [1] E. A. Olivetti, G. Ceder, G. G. Gaustad, and X. Fu, Lithium-Ion Battery Supply Chain Considerations: Analysis of Potential Bottlenecks in Critical Metals, *Joule* **1**, 229 (2017).
- [2] L. Xie, C. Singh, S. K. Mitter, M. A. Dahleh, and S. S. Oren, Toward carbon-neutral electricity and mobility: Is the grid infrastructure ready?, *Joule* **5**, 1908 (2021).
- [3] Y. Tian, G. Zeng, A. Rutt, T. Shi, H. Kim, J. Wang, J. Koettgen, Y. Sun, B. Ouyang, T. Chen, Z. Lun, Z. Rong, K. Persson, and G. Ceder, Promises and Challenges of Next-Generation “Beyond Li-ion” Batteries for Electric Vehicles and Grid Decarbonization, *Chemical Reviews* **121**, 1623 (2021).
- [4] R. J. Clément, Z. Lun, and G. Ceder, Cation-disordered rocksalt transition metal oxides and oxyfluorides for high energy lithium-ion cathodes, *Energy & Environmental Science* **13**, 345 (2020).
- [5] D.-H. Kwon, J. Lee, N. Artrith, H. Kim, L. Wu, Z. Lun, Y. Tian, Y. Zhu, and G. Ceder, The Impact of Surface Structure Transformations on the Performance of Li-Excess Cation-Disordered Rocksalt Cathodes, *Cell Reports Physical Science* **1**, 100187 (2020).
- [6] L. Li, Z. Lun, D. Chen, Y. Yue, W. Tong, G. Chen, G. Ceder, and C. Wang, Fluorination-Enhanced Surface Stability of Cation-Disordered Rocksalt Cathodes for Li-Ion Batteries, *Advanced Functional Materials* **31**, 2101888 (2021).
- [7] K. Zhou, Y. Li, S. Zheng, M. Zhang, C. Zhang, C. Battaglia, H. Liu, K. Wang, P. Yan, J. Liu, and Y. Yang, Tailoring the redox-active transition metal content to enhance cycling stability in cation-disordered rock-salt oxides, *Energy Storage Materials* **43**, 275 (2021).
- [8] J. Ahn, R. Giovine, V. C. Wu, K. P. Koirala, C. Wang, R. J. Clément, and G. Chen, Ultrahigh-Capacity Rocksalt Cathodes Enabled by Cycling-Activated Structural Changes, *Advanced Energy Materials* **13**, 1 (2023).
- [9] Z. Cai, B. Ouyang, H.-M. Hau, T. Chen, R. Giovine, K. P. Koirala, L. Li, H. Ji, Y. Ha, Y. Sun, J. Huang, Y. Chen, V. Wu, W. Yang, C. Wang, R. J. Clément, Z. Lun, and G. Ceder, In situ formed partially disordered phases as earth-abundant Mn-rich cathode materials, *Nature Energy* **9**, 27 (2023).
- [10] A. Urban, J. Lee, and G. Ceder, The configurational space of rocksalt-type oxides for high-capacity lithium battery electrodes, *Advanced Energy Materials* **4**, 1 (2014).
- [11] J. Reed, G. Ceder, and A. Van Der Ven, Layered-to-Spinel Phase Transition in Li_xMnO_2 , *Electrochemical and Solid-State Letters* **4**, A78 (2001).
- [12] Y.-I. Jang, F. Chou, B. Huang, D. R. Sadoway, and Y.-M. Chiang, Magnetic characterization of orthorhombic LiMnO_2 and electrochemically transformed spinel Li_xMnO_2 ($x < 1$), *Journal of Physics and Chemistry of Solids* **64**, 2525–2533 (2003).
- [13] M. R. Jo, Y. Kim, J. Yang, M. Jeong, K. Song, Y.-I. Kim, J.-M. Lim, M. Cho, J.-H. Shim, Y.-M. Kim, W.-S. Yoon, and Y.-M. Kang, Triggered reversible phase transformation between layered and spinel structure in manganese-based layered compounds, *Nature Communications* **10**, 3385 (2019).
- [14] M. D. Radin, J. Vinkeviciute, R. Seshadri, and A. Van der Ven, Manganese oxidation as the origin of the anomalous capacity of Mn-containing Li-excess cathode materials, *Nature Energy* **4**, 639 (2019).
- [15] A. G. Squires and D. O. Scanlon, Understanding the lim-

- its to short-range order suppression in many-component disordered rock salt lithium-ion cathode materials, *Journal of Materials Chemistry A* **11**, 13765 (2023).
- [16] B. Puchala, J. C. Thomas, A. R. Natarajan, J. G. Goiri, S. S. Behara, J. L. Kaufman, and A. Van der Ven, CASM – A software package for first-principles based study of multicomponent crystalline solids, *Computational Materials Science* **217**, 111897 (2023).
- [17] P. Zhong, F. Xie, L. Barroso-Luque, L. Huang, and G. Ceder, Modeling intercalation chemistry with multi-redox reactions by sparse lattice models in disordered rocksalt cathodes, *PRX Energy* **2**, 043005 (2023).
- [18] T. Chen, J. Yang, L. Barroso-Luque, and G. Ceder, Removing the Two-Phase Transition in Spinel LiMn_2O_4 through Cation Disorder, *ACS Energy Letters* **8**, 314 (2023).
- [19] S. Batzner, A. Musaelian, L. Sun, M. Geiger, J. P. Mailoa, M. Kornbluth, N. Molinari, T. E. Smidt, and B. Kozinsky, E(3)-equivariant graph neural networks for data-efficient and accurate interatomic potentials, *Nature Communications* **13**, 2453 (2022).
- [20] C. Chen and S. P. Ong, A universal graph deep learning interatomic potential for the periodic table, *Nature Computational Science* **2**, 718 (2022).
- [21] B. Deng, P. Zhong, K. Jun, J. Riebesell, K. Han, C. J. Bartel, and G. Ceder, CHGNet as a pretrained universal neural network potential for charge-informed atomistic modelling, *Nature Machine Intelligence* **5**, 1031 (2023).
- [22] J. Gilmer, S. S. Schoenholz, P. F. Riley, O. Vinyals, and G. E. Dahl, Neural message passing for quantum chemistry, in *International conference on machine learning* (PMLR, 2017) pp. 1263–1272.
- [23] J. Riebesell, R. E. A. Goodall, P. Benner, Y. Chiang, B. Deng, G. Ceder, M. Asta, A. A. Lee, A. Jain, and K. A. Persson, A framework to evaluate machine learning crystal stability predictions, *Nature Machine Intelligence* **7**, 836–847 (2025).
- [24] B. Deng, Y. Choi, P. Zhong, J. Riebesell, S. Anand, Z. Li, K. Jun, K. A. Persson, and G. Ceder, Systematic softening in universal machine learning interatomic potentials, *npj Computational Materials* **11**, 9 (2025).
- [25] A. D. Kaplan, R. Liu, J. Qi, T. W. Ko, B. Deng, J. Riebesell, G. Ceder, K. A. Persson, and S. P. Ong, A foundational potential energy surface dataset for materials, *arXiv 10.48550/arxiv.2503.04070* (2025).
- [26] M. L. H. Chandrappa, J. Qi, C. Chen, S. Banerjee, and S. P. Ong, Thermodynamics and kinetics of the cathode–electrolyte interface in all-solid-state li–s batteries, *Journal of the American Chemical Society* **144**, 18009 (2022).
- [27] A. Jain, S. P. Ong, G. Hautier, W. Chen, W. D. Richards, S. Dacek, S. Cholia, D. Gunter, D. Skinner, G. Ceder, and K. A. Persson, Commentary: The Materials Project: A materials genome approach to accelerating materials innovation, *APL Materials* **1**, 011002 (2013).
- [28] H. Ji, A. Urban, D. A. Kitchaev, D.-H. Kwon, N. Artrith, C. Ophus, W. Huang, Z. Cai, T. Shi, J. C. Kim, H. Kim, and G. Ceder, Hidden structural and chemical order controls lithium transport in cation-disordered oxides for rechargeable batteries, *Nature Communications* **10**, 592 (2019).
- [29] B. Ouyang, N. Artrith, Z. Lun, Z. Jadidi, D. A. Kitchaev, H. Ji, A. Urban, and G. Ceder, Effect of Fluorination on Lithium Transport and Short-Range Order in Disordered-Rocksalt-Type Lithium-Ion Battery Cathodes, *Advanced Energy Materials* **10**, 1903240 (2020).
- [30] L. Wang, T. Maxisch, and G. Ceder, A first-principles approach to studying the thermal stability of oxide cathode materials, *Chemistry of materials* **19**, 543 (2007).
- [31] J. Lee, A. Urban, X. Li, D. Su, G. Hautier, and G. Ceder, Unlocking the Potential of Cation-Disordered Oxides for Rechargeable Lithium Batteries, *Science* **343**, 519 (2014).
- [32] J. Reed, G. Ceder, and A. V. D. Ven, Layered-to-Spinel Phase Transition in Li_xMnO_2 , *Electrochemical and Solid-State Letters* **4**, A78 (2001).
- [33] Y. Huang, Y. Dong, S. Li, J. Lee, C. Wang, Z. Zhu, W. Xue, Y. Li, and J. Li, Lithium Manganese Spinel Cathodes for Lithium-Ion Batteries, *Advanced Energy Materials* **11**, 2000997 (2021).
- [34] F. Zhou, M. Cococcioni, C. A. Marianetti, D. Morgan, and G. Ceder, First-principles prediction of redox potentials in transition-metal compounds with LDA+ U , *Physical Review B* **70**, 235121 (2004), 0406382.
- [35] S. Swathilakshmi, R. Devi, and G. Sai Gautam, Performance of the r 2 SCAN Functional in Transition Metal Oxides, *Journal of Chemical Theory and Computation* **19**, 4202 (2023).
- [36] J. Sun, A. Ruzsinszky, and J. P. Perdew, Strongly Constrained and Appropriately Normed Semilocal Density Functional, *Physical Review Letters* **115**, 036402 (2015).
- [37] P. Zhong, Z. Cai, Y. Zhang, R. Giovine, B. Ouyang, G. Zeng, Y. Chen, R. Clément, Z. Lun, and G. Ceder, Increasing capacity in disordered rocksalt cathodes by mg doping, *Chemistry of Materials* **32**, 10728 (2020).
- [38] T. Holstun, T. P. Mishra, L. Huang, H. Hau, S. Anand, X. Yang, C. Ophus, K. Bustillo, L. Ma, S. Ehrlich, and G. Ceder, Accelerating the Electrochemical Formation of the δ Phase in Manganese-Rich Rocksalt Cathodes, *Advanced Materials* **37**, 1 (2025).
- [39] H.-M. Hau, T. Mishra, C. Ophus, T.-Y. Huang, K. Bustillo, Y. Sun, X. Yang, T. Holstun, X. Zhao, S. Wang, Y. Ha, G.-H. Lee, C. Song, J. Turner, J. Bai, L. Ma, K. Chen, F. Wang, W. Yang, B. D. McCloskey, Z. Cai, and G. Ceder, Earth-abundant Li-ion cathode materials with nanoengineered microstructures, *Nature Nanotechnology* 10.1038/s41565-024-01787-y (2024).
- [40] P. Xiao, T. Shi, W. Huang, and G. Ceder, Understanding surface densified phases in ni-rich layered compounds, *ACS Energy Letters* **4**, 811 (2019).
- [41] Z. Deng, T. P. Mishra, W. Xie, D. A. Saeed, G. S. Gautam, and P. Canepa, kmcpy: A python package to simulate transport properties in solids with kinetic monte carlo, *Computational Materials Science* **229**, 112394 (2023).
- [42] J. H. Yang, T. Chen, L. Barroso-Luque, Z. Jadidi, and G. Ceder, Approaches for handling high-dimensional cluster expansions of ionic systems, *npj Computational Materials* **8**, 133 (2022).
- [43] K. Han, B. Deng, A. B. Farimani, and G. Ceder, Distmlip: A distributed inference platform for machine learning interatomic potentials, *arXiv* (2025), 2506.02023.
- [44] H. Zhao, H. D. Deng, A. E. Cohen, J. Lim, Y. Li, D. Fraggedakis, B. Jiang, B. D. Storey, W. C. Chueh, R. D. Braatz, and M. Z. Bazant, Learning heterogeneous reaction kinetics from x-ray videos pixel by pixel, *Nature* **621**, 289 (2023).
- [45] X. Fu, T. Xie, N. J. Rebello, B. D. Olsen, and T. Jaakkola, Simulate time-integrated coarse-grained

- molecular dynamics with geometric machine learning, *Transactions on Machine Learning Research (TMLR)* (2022).
- [46] T. Hsu, B. Sadigh, V. Bulatov, and F. Zhou, Score Dynamics: Scaling Molecular Dynamics with Picoseconds Time Steps via Conditional Diffusion Model, *Journal of Chemical Theory and Computation* **20**, 2335 (2024).
- [47] J. Nam, S. Liu, G. Winter, K. Jun, S. Yang, and R. Gómez-Bombarelli, Flow matching for accelerated simulation of atomic transport in materials, arXiv preprint arXiv:2410.01464 (2024).
- [48] Y. Xie, J. Vandermause, S. Ramakers, N. H. Protik, A. Johansson, and B. Kozinsky, Uncertainty-aware molecular dynamics from Bayesian active learning for phase transformations and thermal transport in SiC, *npj Computational Materials* **9**, 36 (2023).
- [49] J. Qi, T. W. Ko, B. C. Wood, T. A. Pham, and S. P. Ong, Robust training of machine learning interatomic potentials with dimensionality reduction and stratified sampling, *npj Computational Materials* **10**, 43 (2024).
- [50] C. Duan, Y. Du, H. Jia, and H. J. Kulik, Accurate transition state generation with an object-aware equivariant elementary reaction diffusion model, arXiv preprint arXiv:2304.06174 (2023).
- [51] G. Kresse and J. Furthmüller, Efficiency of ab-initio total energy calculations for metals and semiconductors using a plane-wave basis set, *Computational Materials Science* **6**, 15 (1996).
- [52] G. Kresse and D. Joubert, From ultrasoft pseudopotentials to the projector augmented-wave method, *Physical Review B* **59**, 1758 (1999).
- [53] J. W. Furness, A. D. Kaplan, J. Ning, J. P. Perdew, and J. Sun, Accurate and Numerically Efficient r²SCAN Meta-Generalized Gradient Approximation, *The Journal of Physical Chemistry Letters* **11**, 8208 (2020), arXiv:2008.03374.
- [54] R. Kingsbury, A. S. Gupta, C. J. Bartel, J. M. Munro, S. Dwaraknath, M. Horton, and K. A. Persson, Performance comparison of r²SCAN and SCAN metaGGA density functionals for solid materials via an automated, high-throughput computational workflow, *Physical Review Materials* **6**, 013801 (2022).
- [55] J. Sanchez, F. Ducastelle, and D. Gratias, Generalized cluster description of multicomponent systems, *Physica A: Statistical Mechanics and its Applications* **128**, 334 (1984).
- [56] C. Wolverton and A. Zunger, First-principles prediction of vacancy order-disorder and intercalation battery voltages in Li_xCoO₂, *Physical Review Letters* **81**, 606 (1998).
- [57] A. van de Walle, Multicomponent multisublattice alloys, nonconfigurational entropy and other additions to the Alloy Theoretic Automated Toolkit, *Calphad* **33**, 266 (2009).
- [58] P. Zhong, T. Chen, L. Barroso-Luque, F. Xie, and G. Ceder, An $\ell_0\ell_2$ -norm regularized regression model for construction of robust cluster expansions in multicomponent systems, *Physical Review B* **106**, 024203 (2022).
- [59] L. Barroso-Luque, P. Zhong, J. H. Yang, F. Xie, T. Chen, B. Ouyang, and G. Ceder, Cluster expansions of multicomponent ionic materials: Formalism and methodology, *Physical Review B* **106**, 144202 (2022).
- [60] L. Barroso-Luque, J. H. Yang, F. Xie, T. Chen, R. L. Kam, Z. Jadidi, P. Zhong, and G. Ceder, smol: A Python package for cluster expansions and beyond, *Journal of Open Source Software* **7**, 4504 (2022).
- [61] S. P. Ong, W. D. Richards, A. Jain, G. Hautier, M. Kocher, S. Cholia, D. Gunter, V. L. Chevrier, K. A. Persson, and G. Ceder, Python Materials Genomics (pymatgen): A robust, open-source python library for materials analysis, *Computational Materials Science* **68**, 314 (2013).